Precise UAV Navigation with Cellular Carrier Phase Measurements

Joe Khalife and Zaher M. Kassas
Department of Electrical and Computer Engineering
University of California, Riverside
Riverside, U.S.A.
joe.khalife@email.ucr.edu, zkassas@ieee.org

***Abstract*—This paper presents two frameworks for precise unmanned aerial vehicle (UAV) navigation with cellular carrier phase measurements. The first framework relies on a mapping UAV and a navigating UAV sharing carrier phase measurements. Experimental results show that a 63.06 cm position root mean-square error (RMSE) is achieved with this framework. The second framework leverages the relative stability of cellular base transceiver station (BTS) clocks, which alleviates the need of a mapper. It was shown through experimental data that the beat frequency stability of cellular BTSs approaches that of atomic standards and may be exploited for precise navigation with cellular carrier phase measurements. Performance bounds are derived for this framework. Experimental data demonstrate a single UAV navigating with sub-meter level accuracy for more than 5 minutes, with one experiment showing 36.61 cm position RMSE and another showing 88.58 cm position RMSE.**

I. Introduction

Unmanned aerial vehicles (UAVs) will demand a resilient, accurate, and tamper-proof navigation system. Current UAV navigation systems will not meet these stringent demands as they are dependent on global navigation satellite system (GNSS) signals, which are jammable, spoofable, and may not be usable in certain environments (e.g., indoors and deep urban canyons) [1]–[3].

The potential of signals of opportunity (SOPs) (e.g., AM/FM radio [4], [5], iridium satellite signals [6], [7], WiFi [8], [9], and cellular [10]–[13]) as alternative navigation sources have been the subject of extensive research recently. Navigation with SOPs has been demonstrated on ground vehicles and UAVs, achieving a localization accuracy ranging from meters to tens of meters, with the latter accuracy corresponding to ground vehicles in deep urban canyons with severe multipath conditions [14]–[17].

Cellular signals, particularly code-division multiple access (CDMA) and long term evolution (LTE), are among the most attractive SOP candidates for navigation. These signals are abundant, received at a much higher power than GNSS signals, offer a favorable horizontal geometry, and are free to use. Several receiver designs have been proposed recently that produce navigation observables from cellular CDMA and LTE signals [18]–[21]. Moreover, error sources pertaining to code phase-based navigation with cellular CDMA systems have been derived and performance under such errors has been characterized [13].

A different challenge that arises in cellular-based navigation is the unknown states of the cellular base transceiver stations (BTSs), namely their position and clock errors (bias and drift). This is in sharp contrast to GNSS-based navigation where the states of the satellites are transmitted to the receiver in the navigation message. To deal with this challenge, a mapper/navigator framework was proposed in [13], [20], where the mapper was assumed to have complete knowledge of its states (e.g., by having access to GNSS signals), estimating the states of BTSs in its environment, and sharing these estimates with a navigator that had no knowledge of its states, making pseudorange measurements on the same BTSs in the environment [13], [20]. Another framework was presented in which the navigator estimated its states simultaneously with the states of the BTSs in the environment, i.e., performed radio simultaneous localization and mapping (radio SLAM) [22]–[26]. It is worth noting that since cellular BTSs are spatially stationary, their positions may be mapped prior to navigation (e.g., by dedicated mapping receivers [27] or from satellite imagery and cellular databases). However, the BTSs' clocks errors must be continuously estimated, whether in the mapper/navigator framework or radio SLAM framework, since these errors are stochastic and dynamic.

The relative stability of cellular CDMA BTSs clocks was recently studied, revealing that while these clocks are not perfectly synchronized to GPS, the clock biases of different neighboring BTSs are dominated by one common term [28]. Moreover, experimental data recorded over 24-hours showed that deviations from this common term are stable processes. These key findings suggest that precise carrier phase navigation with cellular signals is achievable with or without a mapper. This paper presents a comprehensive framework for precise UAV navigation using cellular carrier phase measurements. Experimental results with the proposed framework are presented, demonstrating sub-meter level UAV navigation accuracy. Another contributing factor for achieving such results is that cellular signals received by UAVs do not suffer from severe multipath by virtue of the favorable channel between cellular BTSs and UAVs. This can be seen in the clean correlation functions calculated by the receiver. These results are, to the authors' knowledge, the most accurate navigation

This work was supported in part by the Office of Naval Research (ONR) under Grant N00014-16-1-2305.

results with cellular signals in the published literature. This paper makes three contributions, which are discussed next.

First, two navigation frameworks for precise UAV navigation with cellular carrier phase measurements are developed. The first framework consists of a mapping UAV and a navigating UAV that utilizes carrier phase differential cellular (CD-cellular) measurements. The second framework consists of a single navigating UAV, leveraging the relative stability of the BTS clocks, estimating its position with a weighted nonlinear least-squares (WNLS) estimator.

Second, cellular carrier phase measurements are modeled at a fine granularity level to consist of four terms: true range, common clock error, deviation from the common clock error, and measurement noise. The deviation term is demonstrated to evolve as a stable stochastic process, which is characterized via system identification. Moreover, experimental results over long periods of time validating the identified models are presented. The paper also discusses how to estimate the statistics of this process on-the-fly when the receiver has access to GNSS signals.

Third, the navigation performance for the second framework (single navigating UAV) is characterized. A theoretical lower bound for the logarithm of the determinant of the position estimation error covariance is derived and an upper bound on the position error is provided.

Experimental results are provided demonstrating each of the proposed frameworks. Two sets of experiments are performed where sub-meter level UAV navigation with cellular carrier phase signals is achieved for periods of over five minutes.

The remainder of the paper is organized as follows. Section II describes the cellular carrier phase observable. Section III describes the mapper/navigator framework. Section IV describes the single UAV navigation framework that leverages the relative stability of cellular SOPs. Section V derives stochastic models for the clock deviations and validates these models experimentally. Section VI establishes performance bounds for the second proposed framework. Section VII provides experimental results demonstrating each framework, showing sub-meter level UAV navigation accuracy. Concluding remarks are given in Section VIII.

II. Cellular Carrier Phase Observable Model

In cellular systems, several known signals may be transmitted for synchronization or channel estimation purposes. In CDMA systems, a pilot signal consisting of a pseudorandom noise (PRN) sequence, known as the short code, is modulated by a carrier signal and broadcast by each BTS for synchronization purposes [29]. Therefore, by knowing the shortcode, the receiver may measure the code phase of the pilot signal as well as its carrier phase, hence forming a pseudorange measurement to each BTS transmitting the pilot signal. In LTE, two synchronization signals (primary synchronization signal (PSS) and secondary synchronization signal (SSS)) are broadcast by each evolved node B (eNodeB) [30]. In addition to the PSS and SSS, a reference signal known as the cell-specific reference signal (CRS) is transmitted by each eNodeB for channel estimation purposes [30]. The PSS, SSS, and CRS may be exploited to draw carrier phase and pseudorange measurements on neighboring eNodeBs [21], [31]. In the rest of this paper, availability of code phase and Doppler frequency measurements of cellular CDMA and LTE signals is assumed (e.g., from specialized navigation receivers [19] [20] [12].

The continuous-time carrier phase observable can be obtained by integrating the Doppler measurement over time [32]. The carrier phase (expressed in cycles) made by the i-th receiver on the n-th SOP is given by

$$\phi_n^{(i)}(t) = \phi_n^{(i)}(t_0) + \int_{t_0}^{t} f_{D_n}^{(i)}(\tau)d\tau, \quad n = 1, \ldots, N, \qquad (1)$$

where $f_{D_n}^{(i)}$ is the Doppler measurement made by the i-th receiver on the n-th cellular SOP, $\phi_n^{(i)}(t_0)$ is the initial carrier phase, and N is the total number of SOPs. In (1), i denotes either the mapper M or the navigator N. Assuming a constant Doppler during a subaccumulation period T, (1) can be discretized to yield

$$\phi_n^{(i)}(t_k) = \phi_n^{(i)}(t_0) + \sum_{l=0}^{k-1} f_{D_n}^{(i)}(t_l)T, \qquad (2)$$

where $t_k \triangleq t_0 + kT$. In what follows, the time argument t_k will be replaced by k for simplicity of notation. Note that the receiver will make noisy carrier phase measurements. Adding measurement noise to (2) and expressing the carrier phase observable in meters yields

$$z_n^{(i)}(k) = \lambda\phi_n^{(i)} + \lambda T \sum_{l=0}^{k-1} f_{D_n}^{(i)}(l) + v_n^{(i)}(k), \qquad (3)$$

where λ is the wavelength of the carrier signal and $v_n^{(i)}$ is the measurement noise, which is modeled as a discrete-time zero-mean white Gaussian sequence with variance $\left(\sigma_n^{(i)}\right)^2$, which can be shown for a coherent second-order phase lock loop (PLL) to be given by [32]

$$\left(\sigma_n^{(i)}\right)^2 = \lambda^2 \frac{B_{i,\mathrm{PLL}}}{C/N_{0_n}},$$

where $B_{i,\mathrm{PLL}}$ is the receiver's PLL noise equivalent bandwidth and C/N_{0_n} is the cellular SOP's measured carrier-to-noise ratio. Note that a coherent PLL may be employed in CDMA and LTE navigation receivers since the cellular synchronization and reference signals do not carry any data. The carrier phase in (3) can be parameterized in terms of the receiver and cellular SOP states as

$$\begin{aligned} z_n^{(i)}(k) = {} & \left\|\boldsymbol{r}_{r_i}(k) - \boldsymbol{r}_{s_n}\right\|_2 + c\left[\delta t_{r_i}(k) - \delta t_{s_n}(k)\right] \\ & + \lambda N_n^{(i)} + v_n^{(i)}(k), \end{aligned} \qquad (4)$$

where $\boldsymbol{r}_{r_i} \triangleq [x_{r_i}, y_{r_i}]^{\mathsf{T}}$ is the receiver's position vector; $\boldsymbol{r}_{s_n} \triangleq [x_{s_n}, y_{s_n}]^{\mathsf{T}}$ is the cellular BTS's position vector; c is the speed of light; δt_{r_i} and δt_{s_n} are the receiver's and cellular BTS's clock biases, respectively; and $N_n^{(i)}$ is the carrier phase ambiguity. Note that the difference between the UAV's height and the cellular BTSs' heights is typically negligible compared

to the range between the UAV and the BTSs. Therefore, one may estimate the UAV's two-dimensional (2–D) position only, without introducing significant errors. Moreover, an altimeter may be used to estimate the UAV's height. The subsequent analysis may be readily extended to 3–D; however, the vertical position estimate will suffer from large uncertainties due to the poor vertical diversity of cellular SOPs.

III. Navigation with SOP Carrier Phase Differential Cellular Measurements

In this section, a framework for CD-cellular navigation is developed. The framework consists of two UAVs in an environment comprising N cellular BTSs. The UAVs are assumed to be listening to the same BTSs with the BTS locations being known. The first UAV, referred to as the mapper (M), is assumed to have knowledge of its own position state (e.g., a high-flying UAV with access to GNSS or one equipped with a sophisticated sensor suite). Note that instead of a UAV, the mapper may be a stationary receiver deployed at a surveyed location. The second UAV, referred to as the navigator (N), is assumed only to know its position between $k = 0$ and $k = k_0$ (e.g., from GNSS). For $k > k_0$, the navigator is supposed to subsequently navigate exclusively with cellular carrier phase observables (e.g., its access to GNSS signals was cut off). The mapper communicates its own position and carrier phase observables with the navigator. Fig. 1 illustrates the mapper/navigator framework.

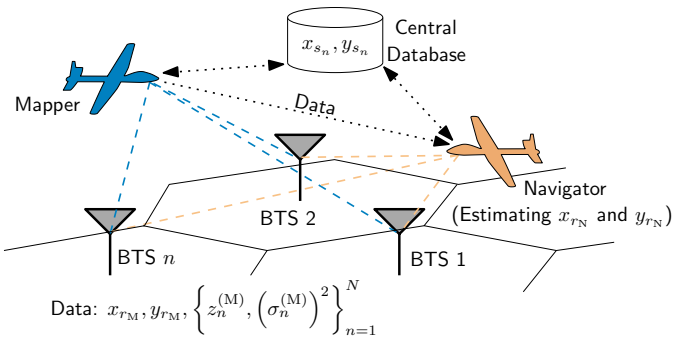

Fig. 1. Mapper/navigator framework.

In what follows, the objective is to estimate the navigator's position, which will be achieved by double-differencing the measurements (4). Without loss of generality, let the measurements to the first SOP be taken as references to form the single difference

$$z_{n,1}^{(i)}(k) \triangleq z_n^{(i)}(k) - z_1^{(i)}(k).$$

Subsequently, define the double difference between N and M as

$$\begin{aligned} z_{n,1}^{(\mathrm{N,M})}(k) &\triangleq z_{n,1}^{(\mathrm{N})}(k) - z_{n,1}^{(\mathrm{M})}(k) \\ &\quad + \|\boldsymbol{r}_{r_\mathrm{M}}(k) - \boldsymbol{r}_{s_n}\|_2 - \|\boldsymbol{r}_{r_\mathrm{M}}(k) - \boldsymbol{r}_{s_1}\|_2 \\ &\triangleq h_{n,1}^{(\mathrm{N})}(k) + \lambda N_{n,1}^{(\mathrm{N,M})} + v_{n,1}^{(\mathrm{N,M})}(k), \end{aligned} \tag{5}$$

where $n = 1, \ldots, N$, $h_{n,1}{}^{(\mathrm{N})}(k) \triangleq \|\boldsymbol{r}_{r_\mathrm{N}}(k) - \boldsymbol{r}_{s_n}\|_2 - \|\boldsymbol{r}_{r_\mathrm{N}}(k) - \boldsymbol{r}_{s_1}\|_2$, $N_{n,1}^{(\mathrm{N,M})} \triangleq N_n^{(\mathrm{N})} - N_n^{(\mathrm{M})} - N_1^{(\mathrm{N})} + N_1^{(\mathrm{M})}$, and $v_{n,1}^{(\mathrm{N,M})}(k) \triangleq v_n^{(\mathrm{N})}(k) - v_n^{(\mathrm{M})}(k) - v_1^{(\mathrm{N})}(k) + v_1^{(\mathrm{M})}(k)$. Define the state to be estimated as the navigator's position $\boldsymbol{x} \triangleq \boldsymbol{r}_{r_\mathrm{N}}$ and the vector of measurements as

$$\boldsymbol{z}(k) \triangleq \boldsymbol{h}\left[\boldsymbol{x}(k)\right] + \lambda \boldsymbol{N} + \boldsymbol{v}(k),$$

where

$$\begin{aligned} \boldsymbol{z}(k) &\triangleq \left[z_{2,1}^{(\mathrm{N,M})}(k), \ldots, z_{M,1}^{(\mathrm{N,M})}(k)\right]^\mathsf{T} \\ \boldsymbol{h}\left[\boldsymbol{x}(k)\right] &\triangleq \left[h_{2,1}^{(\mathrm{N})}(k), \ldots, h_{M,1}^{(\mathrm{N})}(k)\right]^\mathsf{T} \\ \boldsymbol{N} &\triangleq \left[N_{2,1}^{(\mathrm{N,M})}, \ldots, N_{M,1}^{(\mathrm{N,M})}\right]^\mathsf{T} \\ \boldsymbol{v}(k) &\triangleq \left[v_{2,1}^{(\mathrm{N,M})}(k), \ldots, v_{M,1}^{(\mathrm{N,M})}(k)\right]^\mathsf{T}, \end{aligned}$$

where $\boldsymbol{v}(k)$ has a covariance $\mathbf{R}_{\mathrm{N,M}}$ which can be readily shown to be

$$\mathbf{R}_{\mathrm{N,M}} = \mathbf{R}^{(1)} + \left[\left(\sigma_1^{(\mathrm{M})}\right)^2 + \left(\sigma_1^{(\mathrm{N})}\right)^2\right] \boldsymbol{\Xi},$$

where

$$\mathbf{R}^{(1)} \triangleq \mathrm{diag}\left[\left(\sigma_2^{(\mathrm{M})}\right)^2 + \left(\sigma_2^{(\mathrm{N})}\right)^2, \ldots, \left(\sigma_N^{(\mathrm{M})}\right)^2 + \left(\sigma_N^{(\mathrm{N})}\right)^2\right]$$

and $\boldsymbol{\Xi}$ is a matrix of ones. Note that the vector $\boldsymbol{N}$ is now a vector of integers and has to be known to solve for the navigator's position. To this end, the mapper and navigator will leverage the period where they both know their positions to solve for $\boldsymbol{N}$ through an integer least-squares (ILS) estimator. Define $\boldsymbol{y}(k)$ to be

$$\boldsymbol{y}(k) \triangleq \frac{1}{\lambda}\left\{\boldsymbol{z}(k) - \boldsymbol{h}\left[\boldsymbol{x}(k)\right]\right\} = \boldsymbol{N} + \frac{1}{\lambda}\boldsymbol{v}(k).$$

Using all measurements $\{\boldsymbol{y}(k)\}_{k=0}^{k_0}$, one may solve for the float solution of $\boldsymbol{N}$ either using a batch weighted least-squares (LS) estimator or using a recursive LS estimator. Then a decorrelation method can be used to solve for the integer parts. This will yield the estimate $\hat{\boldsymbol{N}}$ and an associated estimation error of $\delta\boldsymbol{N}$ such that $\boldsymbol{N} = \hat{\boldsymbol{N}} + \delta\boldsymbol{N}$ with the estimation error covariance $\mathbf{Q}_{\boldsymbol{N}}$ [33]. For $k > k_0$, define the new measurement $\boldsymbol{z}'(k)$ according to

$$\boldsymbol{z}'(k) \triangleq \boldsymbol{z}(k) - \lambda\hat{\boldsymbol{N}} = \boldsymbol{h}\left[\boldsymbol{x}(k)\right] + \boldsymbol{v}'(k),$$

where $\boldsymbol{v}'(k) \triangleq \boldsymbol{v}(k) + \lambda\delta\boldsymbol{N}$ is a zero-mean random vector with covariance $\mathbf{R}'_{\mathrm{N,M}} = \mathbf{R}_{\mathrm{N,M}} + \lambda^2\mathbf{Q}_{\boldsymbol{N}}$ and $k > k_0$. Subsequently, one may solve for $\boldsymbol{x}(k)$ where $k > k_0$ using a weighted nonlinear LS (WNLS) estimator.

IV. Navigation with SOP Carrier Phase Measurements: Single UAV

The mapper/navigator framework presented above requires the presence of a mapper and a communication channel between the mapper and the navigator. This section discusses a cellular carrier phase navigation framework that alleviates the need of a mapper, i.e., employable on a single UAV. Note that since what follows only pertains to single UAV navigation, the UAV index i will be dropped for simplicity of notation.

The terms $c\left[\delta t_r(k) - \delta t_{s_n}(k) + \frac{\lambda}{c} N_n\right]$ are combined into one term defined as

$$c\delta t_n(k) \triangleq c\left[\delta t_r(k) - \delta t_{s_n}(k) + \frac{\lambda}{c} N_n\right].$$

It was noted in [28] that cellular BTSs possess tighter carrier frequency synchronization then time (code phase) synchronization (the code phase synchronization requirement as per the cellular protocol is to be within 3 μs). Therefore, the resulting clock biases in the carrier phase estimates will be very similar, up to an initial bias, as shown in Fig. 2. Consequently, one may leverage this relative frequency stability to eliminate parameters that need to be estimated. Moreover, this allows one to use a static estimator (e.g., a WNLS) to estimate the position of the UAV. To achieve this, in what follows, the carrier phase measurement is first re-parameterized and a WNLS estimation framework is subsequently developed.

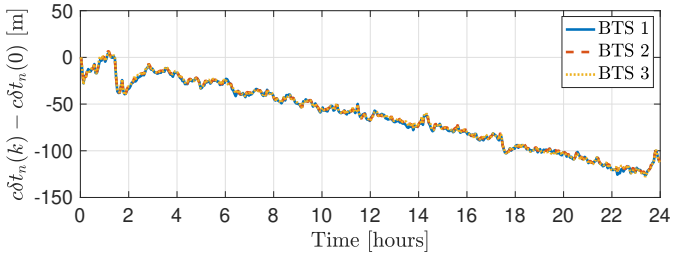

Fig. 2. Experimental data showing $c\delta t_n(k) - c\delta t_n(0)$ obtained from carrier phase measurements over 24 hours for three neighboring BTSs. It can be seen that the clock biases $c\delta t_n(k)$ in the carrier phase measurement are very similar up to an initial bias $c\delta t_n(0)$ which has been removed.

A. Carrier Phase Measurement Re-Parametrization

Motivated by the experimental results in [28], the following re-parametrization is proposed

$$c\bar{\delta t}_n(k) \triangleq c\delta t_n(k) - c\delta t_n(0) \equiv c\delta t(k) + \epsilon_n(k), \quad (6)$$

where $c\delta t$ is a time-varying common bias term and ϵ_n is the deviation of $c\bar{\delta t}_n$ from this common bias and is treated as measurement noise. Using (6), the carrier phase measurement (4) can be re-parameterized as

$$z_n(k) = \|\boldsymbol{r}_r(k) - \boldsymbol{r}_{s_n}\|_2 + c\delta t(k) + c\delta t_{0_n} + \eta_n(k), \quad (7)$$

where $c\delta t_{0_n} \triangleq c\delta t_n(0)$ and $\eta_n(k) \triangleq \epsilon_n(k) + v_n(k)$ is the overall measurement noise. The statistics of ϵ_n will be discussed in Section V. Note that $c\delta t_{0_n}$ can be obtained knowing the initial position and given the initial measurement $z_n(0)$ according to $c\delta t_{0_n} \approx z_n(0) - \|\boldsymbol{r}_r(0) - \boldsymbol{r}_{s_n}\|_2$. This approximation ignores the contribution of the initial measurement noise. If the receiver is initially stationary for a period $k_0 T$ seconds, which is short enough such that $\delta t(k) \approx 0$ for $k = 1, \ldots, k_0$, then the first k_0 samples may be averaged to obtain a more accurate estimate of $c\delta t_{0_n}$.

It is proposed that instead of lumping all N clock biases into one bias $c\delta t$ to be estimated, several clusters of clocks get formed, each of size N_l (i.e., $\sum_{l=1}^{L} N_l = N$, where L is the total number of clusters), and the clocks in each cluster are lumped into one bias $c\delta t_l$ to be estimated. This gives finer granularity for the parametrization (6), since naturally, certain groups of cellular SOPs will be more synchronized with each other than with other groups (e.g., corresponding to the same network provider, transmission protocol, etc.). An illustrative experimental plot is shown in Fig. 3. Note that since the 2–D position vector of the UAV is being estimated along with L clock biases, the number of clusters L cannot exceed $N - 2$, otherwise there would be more unknowns than measurements.

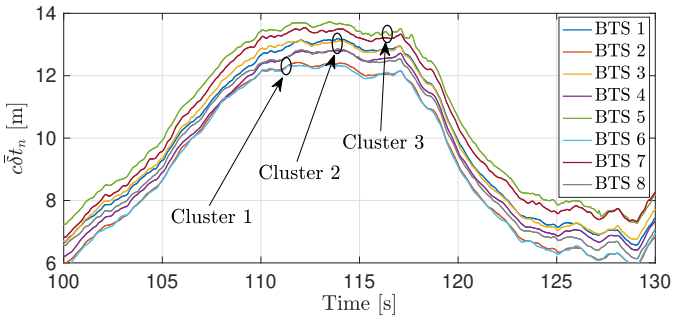

Fig. 3. Experimental data for $c\bar{\delta t}_n(k)$ over 30 seconds for 8 BTSs. The clock biases have been visually clustered into three clusters as an illustrative example.

Without loss of generality, it assumed that the carrier phase measurements have been ordered such that the first N_1 measurements were grouped into the first cluser, the second N_2 measurements were grouped into the second cluster, and so on. Next, obtaining the navigation solution with a WNLS is discussed.

B. Navigation Solution

Given $N \geq 3$ pseudoranges modeled according to (7) and $L \leq N - 2$ SOP clusters, the receiver may solve for its current position $\boldsymbol{r}_r$ and the current set of common biases $c\boldsymbol{\delta t} \triangleq [c\delta t_1, \ldots, c\delta t_L]^\mathsf{T}$ using a WNLS estimator. The state to be estimated is defined by $\boldsymbol{x} \triangleq \left[\boldsymbol{r}_r^\mathsf{T}, c\boldsymbol{\delta t}^\mathsf{T}\right]^\mathsf{T}$. An estimate $\hat{\boldsymbol{x}}$ may be obtained using the iterated WNLS equations given by

$$\hat{\boldsymbol{x}}^{(j+1)}(k) = \hat{\boldsymbol{x}}^{(j)}(k) + \left(\mathbf{H}^\mathsf{T}\mathbf{R}_\eta^{-1}\mathbf{H}\right)^{-1}\mathbf{H}^\mathsf{T}\mathbf{R}_\eta^{-1}\delta\boldsymbol{z}(k), \quad (8)$$

where $\delta\boldsymbol{z}(k) \triangleq [\delta z_1(k), \ldots, \delta z_N(k)]^\mathsf{T}$ and $\delta z_n(k) \triangleq z_n(k) - \left[\left\|\hat{\boldsymbol{r}}_r^{(j)}(k) - \boldsymbol{r}_{s_n}\right\|_2 + c\hat{\delta t}_{l_n}^{(j)}(k) + c\delta t_{0_n}\right]$, $\mathbf{R}_\eta = \mathrm{diag}\left[\sigma_1^2 + \sigma_{\epsilon_1}^2, \ldots, \sigma_N^2 + \sigma_{\epsilon_N}^2\right]$ is the measurement noise covariance where $\sigma_{\epsilon_n}^2$ will be discussed in Section V, j is the WNLS iteration index, and $\mathbf{H}$ is the measurement Jacobian given by

$$\mathbf{H} \triangleq [\mathbf{G} \quad \boldsymbol{\Gamma}], \qquad \boldsymbol{\Gamma} \triangleq \begin{bmatrix} \mathbf{1}_{N_1} & \ldots & \mathbf{0} \\ \vdots & \ddots & \vdots \\ \mathbf{0} & \ldots & \mathbf{1}_{N_L} \end{bmatrix}, \quad (9)$$

$$\mathbf{G} \triangleq \begin{bmatrix} \dfrac{\hat{\boldsymbol{r}}_r^{(j)} - \boldsymbol{r}_{s_1}}{\left\|\hat{\boldsymbol{r}}^{(j)} - \boldsymbol{r}_{s_1}\right\|_2} & \ldots & \dfrac{\hat{\boldsymbol{r}}_r^{(j)} - \boldsymbol{r}_{s_N}}{\left\|\hat{\boldsymbol{r}}^{(j)} - \boldsymbol{r}_{s_N}\right\|_2} \end{bmatrix}^\mathsf{T}, \quad (10)$$

and $\mathbf{1}_{N_l} \triangleq [1,\ldots,1]^\mathsf{T}$. Note that

$$l_n = \begin{cases} 1, & \text{for } n = 1,\ldots,N_1, \\ 2, & \text{for } n = N_1+1,\ldots,\sum_{l=1}^{2} N_l, \\ \vdots & \quad\vdots \\ L, & \text{for } n = \sum_{l=1}^{L-1} N_l + 1,\ldots,N. \end{cases}$$

After convergence (i.e., $\hat{\boldsymbol{x}}^{(j+1)}(k) \approx \hat{\boldsymbol{x}}^{(j)}(k)$) the final estimate is obtained by setting $\hat{\boldsymbol{x}}(k) \equiv \hat{\boldsymbol{x}}^{(j+1)}(k)$. In the rest of the paper, it is assumed that $\mathbf{H}$ is always full column rank.

C. Common Clock Bias Parametrization

Note that the clock bias clusters $\{c\delta t_l\}_{l=1}^{L}$ are "virtual clock biases", which are introduced to group SOPs whose carrier frequency is more synchronized than others. This would in turn yield more precise measurement models, reducing the estimation error. This subsection parameterizes $c\delta t_l$ as a function of $c\delta t_n$. This parametrization is based on the following theorem.

Theorem IV.1. *Consider $N \geq 3$ carrier phase measurements. Assume that the contribution of the relative clock deviation ϵ_n is much larger than the carrier phase measurement noise v_n and that ϵ_n are uncorrelated with identical variances σ^2. Then, the position error at any time instant $\delta\boldsymbol{r}_r(k)$ due to relative clock deviations is independent of $c\delta t_l$.*

Proof. Denote the measurement noise covariance of $\boldsymbol{\eta} \triangleq [\eta_1 \ldots, \eta_n]^\mathsf{T}$ as $\mathbf{R}_\eta$. It is assumed that the WNLS had converged very closely to the true state in the absence of clock deviations. The clock deviations are then suddenly introduced into the measurements, which will induce an incremental change in the receiver state estimate given by

$$\begin{aligned} \delta\boldsymbol{x}(k) &= -\left(\mathbf{H}^\mathsf{T}\mathbf{R}_\eta^{-1}\mathbf{H}\right)^{-1}\mathbf{H}^\mathsf{T}\mathbf{R}_\eta^{-1}\boldsymbol{\epsilon}(k) \\ &= -\left(\bar{\mathbf{H}}^\mathsf{T}\bar{\mathbf{H}}\right)^{-1}\bar{\mathbf{H}}^\mathsf{T}\bar{\boldsymbol{\epsilon}}(k), \end{aligned}$$

where

$$\bar{\mathbf{H}} \triangleq \mathbf{R}_\eta^{-\frac{1}{2}}\mathbf{H}, \quad \bar{\boldsymbol{\epsilon}}(k) \triangleq \mathbf{R}_\eta^{-\frac{1}{2}}\boldsymbol{\epsilon}(k),$$

and $\boldsymbol{\epsilon} \triangleq [\epsilon_1,\ldots,\epsilon_N]^\mathsf{T}$. The matrix product $\bar{\mathbf{H}}^\mathsf{T}\bar{\boldsymbol{\epsilon}}(k)$ can be further expressed as

$$\bar{\mathbf{H}}^\mathsf{T}\bar{\boldsymbol{\epsilon}}(k) = \begin{bmatrix} \bar{\mathbf{G}}^\mathsf{T} \\ \bar{\boldsymbol{\Gamma}}^\mathsf{T} \end{bmatrix}\bar{\boldsymbol{\epsilon}}(k) = \begin{bmatrix} \bar{\mathbf{G}}^\mathsf{T}\bar{\boldsymbol{\epsilon}}(k) \\ \bar{\boldsymbol{\Gamma}}^\mathsf{T}\bar{\boldsymbol{\epsilon}}(k) \end{bmatrix},$$

where

$$\bar{\mathbf{G}} \triangleq \mathbf{R}_\eta^{-\frac{1}{2}}\mathbf{G}, \quad \bar{\boldsymbol{\Gamma}} \triangleq \mathbf{R}_\eta^{-\frac{1}{2}}\boldsymbol{\Gamma}.$$

Next, $\left(\bar{\mathbf{H}}^\mathsf{T}\bar{\mathbf{H}}\right)^{-1}$ is expressed as

$$\left(\bar{\mathbf{H}}^\mathsf{T}\bar{\mathbf{H}}\right)^{-1} = \begin{bmatrix} \bar{\mathbf{G}}^\mathsf{T}\bar{\mathbf{G}} & \bar{\mathbf{G}}^\mathsf{T}\bar{\boldsymbol{\Gamma}} \\ \bar{\boldsymbol{\Gamma}}^\mathsf{T}\bar{\mathbf{G}} & \bar{\boldsymbol{\Gamma}}^\mathsf{T}\bar{\boldsymbol{\Gamma}} \end{bmatrix}^{-1} \triangleq \begin{bmatrix} \mathbf{A} & \mathbf{B} \\ \mathbf{B}^\mathsf{T} & \mathbf{D} \end{bmatrix},$$

where $\mathbf{A}$ is a 2×2 symmetric matrix, $\mathbf{B}$ is a $2\times L$ matrix, and $\mathbf{D}$ is an $L\times L$ symmetric matrix. The estimation error becomes

$$\delta\boldsymbol{x}(k) = \begin{bmatrix} \delta\boldsymbol{r}_r(k) \\ \delta\left(c\boldsymbol{\delta}t(k)\right) \end{bmatrix} = -\begin{bmatrix} \left(\mathbf{A}\bar{\mathbf{G}}^\mathsf{T} + \mathbf{B}\bar{\boldsymbol{\Gamma}}^\mathsf{T}\right)\bar{\boldsymbol{\epsilon}}(k) \\ \left(\mathbf{B}^\mathsf{T}\bar{\mathbf{G}}^\mathsf{T} + \mathbf{D}\bar{\boldsymbol{\Gamma}}^\mathsf{T}\right)\bar{\boldsymbol{\epsilon}}(k) \end{bmatrix}.$$

Using the matrix block inversion lemma, the following may be obtained

$$\begin{aligned} \mathbf{A} &= \left(\bar{\mathbf{G}}^\mathsf{T}\bar{\boldsymbol{\Psi}}\bar{\mathbf{G}}\right)^{-1} \\ \mathbf{B} &= -\left(\bar{\mathbf{G}}^\mathsf{T}\bar{\boldsymbol{\Psi}}\bar{\mathbf{G}}\right)^{-1}\bar{\mathbf{G}}^\mathsf{T}\bar{\boldsymbol{\Gamma}}\left(\bar{\boldsymbol{\Gamma}}^\mathsf{T}\bar{\boldsymbol{\Gamma}}\right)^{-1} \\ \mathbf{D} &= \left(\bar{\boldsymbol{\Gamma}}^\mathsf{T}\bar{\boldsymbol{\Gamma}}\right)^{-1}\left[\mathbf{I} + \bar{\boldsymbol{\Gamma}}^\mathsf{T}\bar{\mathbf{G}}\left(\bar{\mathbf{G}}^\mathsf{T}\bar{\boldsymbol{\Psi}}\bar{\mathbf{G}}\right)^{-1}\bar{\mathbf{G}}^\mathsf{T}\bar{\boldsymbol{\Gamma}}\left(\bar{\boldsymbol{\Gamma}}^\mathsf{T}\bar{\boldsymbol{\Gamma}}\right)^{-1}\right], \end{aligned}$$

where $\bar{\boldsymbol{\Psi}} \triangleq \mathbf{I} - \bar{\boldsymbol{\Gamma}}\left(\bar{\boldsymbol{\Gamma}}^\mathsf{T}\bar{\boldsymbol{\Gamma}}\right)^{-1}\bar{\boldsymbol{\Gamma}}^\mathsf{T}$. This yields the position error given by

$$\delta\boldsymbol{r}_r(k) = -\left(\bar{\mathbf{G}}^\mathsf{T}\bar{\boldsymbol{\Psi}}\bar{\mathbf{G}}\right)^{-1}\bar{\mathbf{G}}^\mathsf{T}\bar{\boldsymbol{\Psi}}\bar{\boldsymbol{\epsilon}}(k).$$

When $\mathbf{R}_\eta = \sigma^2\mathbf{I}$, the above simplifies to

$$\delta\boldsymbol{r}_r(k) = -\left(\mathbf{G}^\mathsf{T}\boldsymbol{\Psi}\mathbf{G}\right)^{-1}\mathbf{G}^\mathsf{T}\boldsymbol{\Psi}\boldsymbol{\epsilon}(k), \tag{11}$$

$$\boldsymbol{\epsilon}(k) \triangleq [\epsilon_1(k),\ldots,\epsilon_N(k)]^\mathsf{T}, \quad \boldsymbol{\Psi} \triangleq \mathbf{I} - \boldsymbol{\Gamma}\left(\boldsymbol{\Gamma}^\mathsf{T}\boldsymbol{\Gamma}\right)^{-1}\boldsymbol{\Gamma}^\mathsf{T}. \tag{12}$$

Note that $\boldsymbol{\Psi}$ is the annihilator matrix of $\boldsymbol{\Gamma}$ and satisfies $\boldsymbol{\Psi}\boldsymbol{\Psi} = \boldsymbol{\Psi}$. It can be readily shown that

$$\boldsymbol{\Psi} = \operatorname{diag}\left[\mathbf{I}_{N_1} - \frac{1}{N_1}\mathbf{1}_{N_1}\mathbf{1}_{N_1}^\mathsf{T}, \ldots, \mathbf{I}_{N_L} - \frac{1}{N_L}\mathbf{1}_{N_L}\mathbf{1}_{N_L}^\mathsf{T}\right].$$

Consequently, (11) implies that the effect on the position error $\delta\boldsymbol{r}_r$ comes from the vector

$$\tilde{\boldsymbol{\epsilon}}(k) \triangleq \boldsymbol{\Psi}\boldsymbol{\epsilon}(k) = -\begin{bmatrix} \boldsymbol{\epsilon}_1(k) - \mu_1(k)\mathbf{1}_{N_1} \\ \vdots \\ \boldsymbol{\epsilon}_L(k) - \mu_L(k)\mathbf{1}_{N_L} \end{bmatrix},$$

where $\boldsymbol{\epsilon}(k) = \left[\boldsymbol{\epsilon}_1^\mathsf{T}(k),\ldots,\boldsymbol{\epsilon}_L^\mathsf{T}(k)\right]^\mathsf{T}$, $\boldsymbol{\epsilon}_l(k) = \left[\epsilon_{l_1},\ldots,\epsilon_{l_{N_l}}\right]^\mathsf{T}$, and $\mu_l(k) \triangleq \frac{1}{N_l}\sum_{i=1}^{N_l}\epsilon_{l_i}(k)$. Noting that $\epsilon_n(k) = c\delta t_{l_n}(k) - c\bar{\delta}t_n(k)$, the following holds

$$\begin{aligned} \tilde{\epsilon}_n(k) &= \frac{1}{N_l}\sum_{i=1}^{N_l}\left[c\delta t_l(k) - c\bar{\delta}t_{l_i}(k)\right] - \left[c\delta t_l(k) - c\bar{\delta}t_n(k)\right] \\ &= c\bar{\delta}t_n(k) - \frac{1}{N_l}\sum_{i=1}^{N_l}c\bar{\delta}t_{l_i}(k), \end{aligned} \tag{13}$$

which is independent of $c\delta t_l(k)$. ∎

The assumption that the contribution of the relative clock deviation ϵ_n is much larger than the carrier phase measurement noise v_n comes from experimental data, where $\|\boldsymbol{\epsilon}\|_2$ was observed to be within 0.2 and 4 m, whereas σ_n was on the order of a few cm. Form Theorem IV.1, it can be implied that while the position error is independent of $c\delta t_l$, it depends on the clustering. Following the result in (13), the following parametrization is adopted

$$c\delta t_l(k) \equiv \frac{1}{N_l}\sum_{i=1}^{N_l}c\bar{\delta}t_{l_i}(k), \quad \epsilon_n(k) \equiv c\bar{\delta}t_n(k) - c\delta t_l(k). \tag{14}$$

The following section models the dynamics of ϵ_n.

V. Frequency Stability and Modeling the Dynamics of Clock Deviations

In this section, the frequency stability and the deviations ϵ_n in cellular CDMA systems are characterized.

A. Observed Frequency Stability in Cellular CDMA Systems

In order to study the stability of cellular CDMA BTS clocks, real CDMA signals were collected over a period of 24 hours via a stationary universal software radio peripheral (USRP) driven by a GPS-disciplined oscillator (GPSDO). Since the USRP clock is driven by a GPSDO, the apparent Doppler frequency will be mainly caused by the drift in the BTS clock. The Allan deviations were calculated for each BTS using: (1) the absolute Doppler frequencies and (2) the beat Doppler frequencies. The absolute Doppler frequencies are the frequencies directly observed by the receiver on each BTS. The beat Doppler frequency is defined as

$$f_{bD_n} \triangleq f_{D_n} - \frac{1}{N}\sum_{n=1}^{N} f_{D_n},$$

following the parametrization in (14). The Allan deviations of the absolute and beat frequencies for three cellular CDMA BTSs nearby the campus of the University of California, Riverside (UCR) are shown in Fig. 4. Note that the absolute and beat Doppler frequencies were normalized by the nominal carrier frequency f_c; hence, the Allan deviations are unitless.

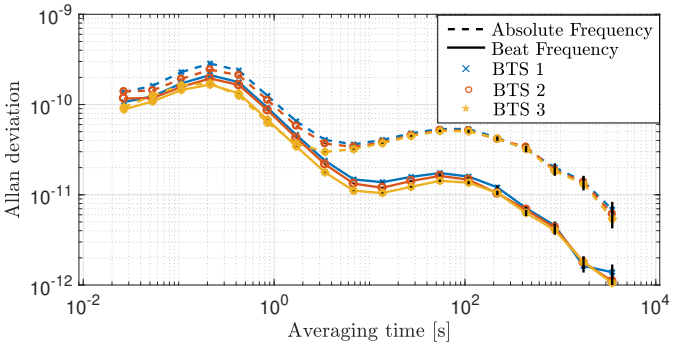

Fig. 4. Allan deviations of absolute and beat frequencies for three CDMA BTSs near UCR. The Allan deviations were calculated from data collected over 24 hours. The carrier frequency was $f_c = 883.98$ MHz.

Two main conclusions may be drawn from Fig. 4. First, the beat frequencies are an order of magnitude more stable than the absolute frequencies. Second, the stability of the beat frequencies approaches that of atomic standards for periods of hundreds to a few thousands seconds. This implies that cellular CDMA signals may be exploited for precise navigation for several minutes using carrier phase measurements.

A similar experiment was conducted at a different time in Colton, California. However, only ten minutes of data were collected. The Allan deviations for two cellular CDMA BTSs in Colton, California, are shown in Fig. 5. Similar conclusions are drawn from Fig. 5.

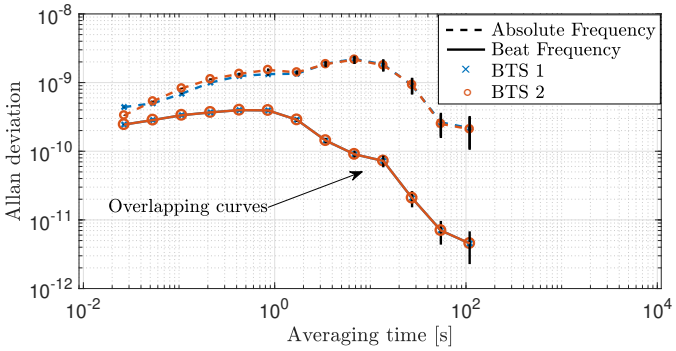

Fig. 5. Allan deviations of absolute and beat frequencies for two CDMA BTSs in Colton, California. The Allan deviations were calculated from data collected over ten minutes. The carrier frequency was $f_c = 882.75$ MHz.

B. Modeling the Dynamics of Clock Deviations

Fig. 6 shows the clock bias deviations $\{\epsilon_n\}_{n=1}^{3}$ for the three cellular BTSs nearby UCR over 24 hours.

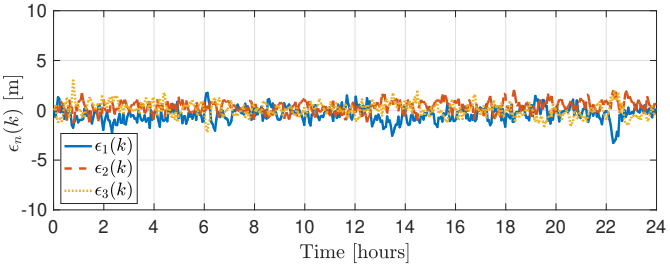

Fig. 6. Plot of the deviations $\epsilon_n(k)$ from the common clock bias for three BTSs near UCR over 24 hours.

The UAV can perform an exhaustive search over the different clustering possibilities to minimize its position error while it has access to GPS. The number of possible clusters is given by $N_{\text{clus}} = \sum_{L=1}^{N-2} \binom{N}{L} = \sum_{L=1}^{N-2} \frac{N!}{L!(N-L)!}$. It can be seen that this number becomes impractically large as N increases. A rule-of-thumb that significantly reduces N_{num} is discussed in Subsection VI-C. Subsequently, it is assumed that a clustering is given. Next, ϵ_n are calculated according to (14). It can be seen from Fig. 6 that ϵ_n is bounded. It can be readily verified (e.g., through spectral analysis) that ϵ_n is not a white sequence. An auto regressive moving average (ARMA) model is proposed to describe the dynamics of ϵ_n, which is generically expressed as

$$\epsilon_n(k+1) = \sum_{i=1}^{p} \phi_i \epsilon_n(k-i+1) + \sum_{i=1}^{q} \psi_i w_{\epsilon_n}(k-i+1) + w_{\epsilon_n}(k), \tag{15}$$

where p and $\{\phi_i\}_{i=1}^{p}$ are the order and the coefficients of the autoregressive (AR) part, respectively; q and $\{\psi_i\}_{i=1}^{q}$ are the order and the coefficients of the moving average (MA) part, respectively; and w_ϵ is a white sequence. Identifying p and q and their corresponding coefficients can be readily obtained with standard system identification techniques [34]. Here, the MATLAB System Identification Toolbox was used to identify (15), where it was found that $p = q = 6$ was usually enough to whiten w_{ϵ_n}.

C. Statistics of the Residuals

In this subsection, the resulting residuals w_ϵ are studied. To this end, the autocorrelation function (acf) and the probability density function (pdf) of the residuals are computed for the three realizations of ϵ_n shown in Fig. 6. Note that half of the data was used for system identification and the other half was used to validate the model. The acf and pdf of the residuals obtained with the second half of the data are plotted in Figs. 7(a)–(c). A Gaussian pdf fit (red) was also plotted. It can be seen that $\{w_{\epsilon_n}\}_{n=1}^3$ are zero-mean white Gaussian sequences, with variances $\left\{\sigma^2_{w_{\epsilon_n}}\right\}_{n=1}^3$.

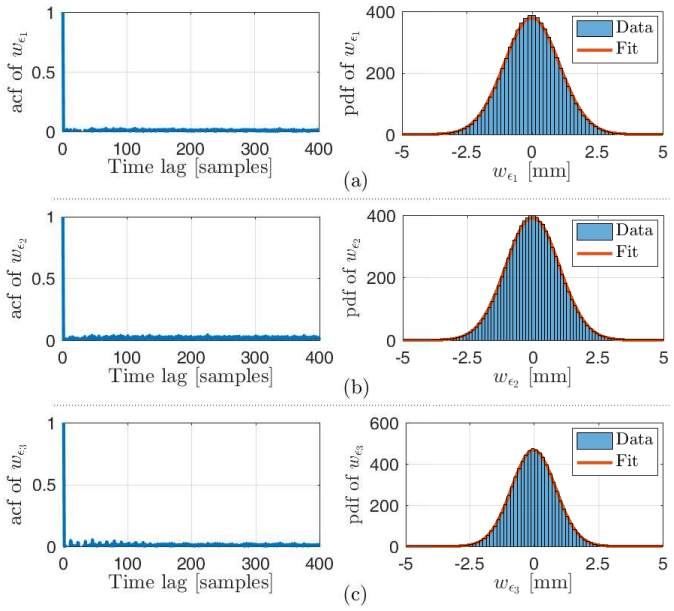

Fig. 7. (a), (b), and (c) show the acfs and pdfs of w_{ϵ_1}, w_{ϵ_2}, and w_{ϵ_3}, respectively. The acfs show that the sequences $\{w_{\epsilon_n}\}_{n=1}^3$ are approximately white and the pdfs show that the sequences are Gaussian.

D. Statistics of the Clock Deviations

Since $w_{\epsilon_n}(k)$ was found to be a Gaussian sequence, then ϵ_n, which is a linear combination of $w_{\epsilon_n}(k)$ will also be Gaussian. Without loss of generality, it is assumed that $\epsilon_n(i-p)=0$ for $i=1,\ldots,p$. Subsequently, $\mathbb{E}\left[\epsilon_n(k)\right]=0$. The variance of $\epsilon_n(k)$ is discussed next. The ARMA process identified earlier may be represented in state-space according to

$$\begin{aligned}\boldsymbol{\xi}_n(k+1) &= \mathbf{F}_{\xi_n}\boldsymbol{\xi}_n(k)+\boldsymbol{\Gamma}_{\xi_n}w_{\epsilon_n}(k)\\ \epsilon_n(k) &= \boldsymbol{h}_{\epsilon_n}^{\mathsf{T}}\boldsymbol{\xi}_n(k)\end{aligned}$$

where $\boldsymbol{\xi}_n$ is the underlying dynamic AR process, $\mathbf{F}_{\xi_n}$ is its state transition matrix, $\boldsymbol{\Gamma}_{\xi_n}$ is the input matrix, and $\boldsymbol{h}_{\epsilon_n}^{\mathsf{T}}$ is the output matrix. The eigenvalues of $\mathbf{F}_{\xi_n}$ were computed to be inside the unit circle, implying stability of $\boldsymbol{\xi}_n$. The covariance of $\boldsymbol{\xi}_n$, denoted $\mathbf{P}_{\xi_n}$, evolves according to

$$\mathbf{P}_{\xi_n}(k+1)=\mathbf{F}_{\xi_n}\mathbf{P}_{\xi_n}(k)\mathbf{F}_{\xi_n}^{\mathsf{T}}+\mathbf{Q}_{\xi_n},$$

where $\mathbf{Q}_{\xi_n}\triangleq\sigma^2_{w_{\epsilon_n}}\boldsymbol{\Gamma}_{\xi_n}\boldsymbol{\Gamma}_{\xi_n}^{\mathsf{T}}$ and the variance of the clock deviation ϵ_n at any given time-step is given by

$$\sigma^2_{\epsilon_n}(k)=\boldsymbol{h}_{\epsilon_n}^{\mathsf{T}}\mathbf{P}_{\xi_n}(k)\boldsymbol{h}_{\epsilon_n}.$$

Since $\boldsymbol{\xi}_n$ is stable, $\mathbf{P}_{\xi_n}(k)$ will converge to a finite steady-state covariance denoted $\mathbf{P}_{\xi_n,\mathrm{ss}}$ given by the solution to the discrete-time matrix Lyapunov equation

$$\mathbf{P}_{\xi_n,\mathrm{ss}}=\mathbf{F}_{\xi_n}\mathbf{P}_{\xi_n,\mathrm{ss}}\mathbf{F}_{\xi_n}^{\mathsf{T}}+\mathbf{Q}_{\xi_n}.$$

Subsequently, the steady-state variance of the clock deviation is given by

$$\sigma^2_{\epsilon_n}=\boldsymbol{h}_{\epsilon_n}^{\mathsf{T}}\mathbf{P}_{\xi_n,\mathrm{ss}}\boldsymbol{h}_{\epsilon_n}.$$

VI. Performance Characterization

This section derives performance bounds for the single UAV navigation framework using SOP carrier phase measurements presented in Section IV. Also, clustering of the clock bias biases is investigated and an upper bound on the position error is derived.

A. A Note on the Optimal BTS Geometric Configuration

The measurement Jacobian $\mathbf{G}$ with respect to the position states (cf. (10)) could be re-parameterized in terms of the bearing angles θ_n between each SOP and the UAV, given by

$$\mathbf{G}=\begin{bmatrix}\cos\theta_1 & \ldots & \cos\theta_N\\ \sin\theta_1 & \ldots & \sin\theta_N\end{bmatrix}^{\mathsf{T}},$$

as illustrated in Fig. 8(a). The optimal geometric configuration of sensors (or navigation sources) around an emitter (or receiver) has been well studied in the literature. This problem is also similar to the geometric dilution of precision (GDOP) minimization problem in GPS. It was found that the GDOP is minimized when the end points of the unit line of sight vectors pointing from the receiver to each navigation source form a regular polygon around the receiver, as shown in Fig. 8(b). In the sequel, the aforementioned configuration will be referred to as the optimal configuration, where the bearing angles are given by $\theta_n=\frac{2\pi(n-1)}{N}$, $n=1,\ldots,N$. Note that these results hold for $N\geq 3$ in the 2-D case.

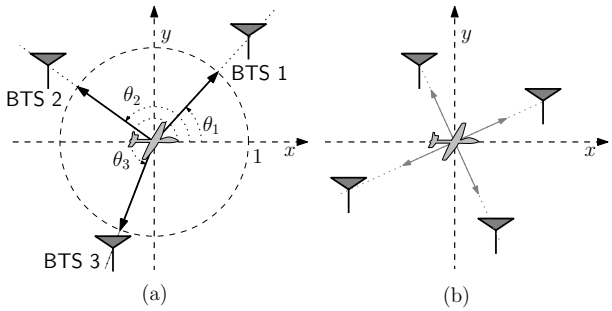

Fig. 8. (a) Re-parametrization of the measurement Jacobian as a function of the bearing angles θ_n. (b) Optimal geometric configuration of the BTSs around the receiver.

B. Lower Bound on the logarithm of the Determinant of the Position Estimation Error Covariance

It can be readily seen that optimal performance is achieved when all clocks are perfectly synchronized, i.e., $\epsilon_n(k)=0$, $\forall\, k$, and therefore $\mathbf{R}_\eta=\mathbf{R}$. In this case, only one clock bias is estimated, and this problem becomes similar to the one discussed in [13], in which it is shown that the logarithm

of the determinant of the position estimation error covariance $\mathbf{P}_{x,y}$ is bounded by

$$\log\det\left[\mathbf{P}_{x,y}\right] \geq -2\log\left[\mathrm{trace}\left(\mathbf{R}^{-1}\right)\right].$$

C. Clustering of the Clock Biases

It was mentioned in Subsection V-B that an exhaustive search may be performed to cluster the clock biases $c\delta t_n$ in order to minimize the position estimation error. This amounts to finding the matrix $\mathbf{\Gamma}$ that minimizes

$$J_p(\mathbf{\Gamma}) \triangleq \sum_{k=1}^{k_0} \|\delta \boldsymbol{r}_r(k)\|_2^2 =$$

$$\sum_{k=1}^{k_0} \left\| \left[\mathbf{G}^\mathsf{T}\left(\mathbf{I}-\mathbf{\Gamma}\left(\mathbf{\Gamma}^\mathsf{T}\mathbf{\Gamma}\right)^{-1}\mathbf{\Gamma}^\mathsf{T}\right)\mathbf{G}\right]^{-1}\mathbf{G}^\mathsf{T}\left(\mathbf{I}-\mathbf{\Gamma}\left(\mathbf{\Gamma}^\mathsf{T}\mathbf{\Gamma}\right)^{-1}\mathbf{\Gamma}^\mathsf{T}\right)\boldsymbol{\epsilon}(k)\right\|_2^2$$

$$= \sum_{k=1}^{k_0} \left\| \left(\mathbf{G}^\mathsf{T}\mathbf{\Psi}\mathbf{G}\right)^{-1}\mathbf{G}^\mathsf{T}\mathbf{\Psi}\boldsymbol{\epsilon}(k)\right\|_2^2,$$

where $\mathbf{\Gamma}$ and $\mathbf{\Psi}$ are defined in (9) and (12), respectively. This optimization problem is non-convex and intractable. Instead of optimizing $J_p(\mathbf{\Gamma})$, a tractable rule-of-thumb is provided next. First, consider the modified cost function

$$\begin{aligned} J(\mathbf{\Gamma}) &\triangleq \left\| \left(\mathbf{G}^\mathsf{T}\mathbf{\Psi}\mathbf{G}\right)^{-1}\mathbf{G}^\mathsf{T}\mathbf{\Psi}\boldsymbol{\epsilon}(k_0)\right\|_2^2 \\ &= \left\| \left(\mathbf{G}^\mathsf{T}\mathbf{\Psi}\mathbf{\Psi}\mathbf{G}\right)^{-1}\mathbf{G}^\mathsf{T}\mathbf{\Psi}\mathbf{\Psi}\boldsymbol{\epsilon}(k_0)\right\|_2^2 \\ &\leq \left\| \left(\mathbf{G}_\Gamma^\mathsf{T}\mathbf{G}_\Gamma\right)^{-1}\mathbf{G}_\Gamma^\mathsf{T}\right\|_2^2 \|\mathbf{\Psi}\boldsymbol{\epsilon}(k_0)\|_2^2, \end{aligned}$$

where $\mathbf{G}_\Gamma \triangleq \mathbf{\Psi}\mathbf{G}$. Let the singular value decomposition (svd) of $\mathbf{G}_\Gamma$ be

$$\mathbf{G}_\Gamma = \mathbf{U}\mathbf{\Sigma}_\Gamma\mathbf{V}^\mathsf{T},$$

where $\mathbf{U}$ is an $N\times N$ unitary matrix, $\mathbf{V}$ is a 2×2 unitary matrix, and $\mathbf{\Sigma}_\Gamma = \begin{bmatrix}\mathbf{\Sigma} & \mathbf{0}\end{bmatrix}^\mathsf{T}$, where $\mathbf{\Sigma}$ is a nonsingular 2×2 diagonal matrix containing the nonzero singular values of $\mathbf{G}_\Gamma$. It can be readily shown that

$$\left(\mathbf{G}_\Gamma^\mathsf{T}\mathbf{G}_\Gamma\right)^{-1}\mathbf{G}_\Gamma^\mathsf{T} = \mathbf{V}\mathbf{\Sigma}'\mathbf{U}^\mathsf{T}, \tag{16}$$

where $\mathbf{\Sigma}' \triangleq \begin{bmatrix}\mathbf{\Sigma}^{-1} & \mathbf{0}\end{bmatrix}^\mathsf{T}$. This implies that (16) is the svd of $\left(\mathbf{G}_\Gamma^\mathsf{T}\mathbf{G}_\Gamma\right)^{-1}\mathbf{G}_\Gamma^\mathsf{T}$ and its singular values are the inverses of the singular values of $\mathbf{G}_\Gamma$, yielding

$$\left\| \left(\mathbf{G}_\Gamma^\mathsf{T}\mathbf{G}_\Gamma\right)^{-1}\mathbf{G}_\Gamma^\mathsf{T}\right\|_2^2 = \left[\sigma_{\max}\left(\mathbf{G}_\Gamma\right)\right]^2 = \left[\frac{1}{\sigma_{\min}\left(\mathbf{G}_\Gamma\right)}\right]^2,$$

where $\sigma_{\max}(\cdot)$ and $\sigma_{\min}(\cdot)$ denote the maximum and minimum singular values of a matrix, respectively. Note that the singular values of $\mathbf{G}_\Gamma$ are the square root of the eigenvalues of $\mathbf{G}_\Gamma^\mathsf{T}\mathbf{G}_\Gamma = \mathbf{G}^\mathsf{T}\mathbf{\Psi}\mathbf{G}$, and hence

$$\left\| \left(\mathbf{G}_\Gamma^\mathsf{T}\mathbf{G}_\Gamma\right)^{-1}\mathbf{G}_\Gamma^\mathsf{T}\right\|_2^2 = \frac{1}{\lambda_{\min}\left(\mathbf{G}^\mathsf{T}\mathbf{\Psi}\mathbf{G}\right)} = \lambda_{\max}\left(\mathbf{P}_{x,y}\right),$$

where $\lambda_{\max}(\cdot)$ and $\lambda_{\min}(\cdot)$ denote the maximum and minimum eigenvalues of a matrix, respectively. Consequently, the cost $J(\mathbf{\Gamma})$ may be bounded by

$$J(\mathbf{\Gamma}) \leq \lambda_{\max}\left(\mathbf{P}_{x,y}\right)\|\mathbf{\Psi}\boldsymbol{\epsilon}(k_0)\|_2^2. \tag{17}$$

Next, two theorems are presented that will help derive the rule-of-thumb for clustering the clock biases.

Theorem VI.1. *Assume a clock bias clustering with $L < N-2$ clusters and denote $J_L \triangleq \|\mathbf{\Psi}\boldsymbol{\epsilon}(k)\|_2^2$. Then, there exists a clustering with $L+1$ clusters such that $J_L \geq J_{L+1}$.*

Proof. First, note that J_L may be expressed as

$$\begin{aligned} J_L = \|\mathbf{\Psi}\boldsymbol{\epsilon}(k)\|_2^2 &= \left\| \begin{bmatrix} \boldsymbol{\epsilon}_1(k)-\mu_1(k)\mathbf{1}_{N_1} \\ \vdots \\ \boldsymbol{\epsilon}_L(k)-\mu_L(k)\mathbf{1}_{N_L}\end{bmatrix}\right\|_2^2 \\ &= \sum_{l=1}^{L}\|\boldsymbol{\epsilon}_l-\mu_l(k)\mathbf{1}_{N_l}\|_2^2 = \sum_{l=1}^{L}\sum_{j=1}^{N_l}\left[\epsilon_{l_j}(k)-\mu_l(k)\right]^2 \\ &= \sum_{l=1}^{L-1}\sum_{j=1}^{N_l}\left[\epsilon_{l_j}(k)-\mu_l(k)\right]^2 + \sum_{j=1}^{N_L}\left[\epsilon_{L_j}(k)-\mu_l(k)\right]^2 \\ &= a + \sum_{j=1}^{N_L}(\epsilon_{L_j}(k)-\mu_L(k))^2, \end{aligned}$$

where $a \triangleq \sum_{l=1}^{L-1}\sum_{j=1}^{N_l}\left[\epsilon_{l_j}(k)-\mu_l(k)\right]^2$. In what follows, the time argument k will be dropped for simplicity of notation. Now add an additional cluster by partitioning $\boldsymbol{\epsilon}_L$ according to $\boldsymbol{\epsilon}_L = \left[\boldsymbol{\epsilon}'^\mathsf{T}_L, \epsilon_{L+1}\right]^\mathsf{T}$ and define

$$J_{L+1} = a + \sum_{j=1}^{N_L-1}\left(\epsilon_{L_j}-\mu'_L\right)^2 + \left(\epsilon_{L+1}-\mu_{L+1}\right)^2,$$

where $\mu'_L \triangleq \frac{1}{N_L-1}\sum_{j=1}^{N_L-1}\epsilon_{L_j}$ and $\mu_{L+1} = \epsilon_{L+1}$. Subsequently, J_{L+1} may be expressed as

$$J_{L+1} = a + \sum_{j=1}^{N_L-1}(\epsilon_{L_j}-\mu_L)^2.$$

The second term in J_L may be expressed as

$$\begin{aligned} \sum_{j=1}^{N_L}(\epsilon_{L_j}-\mu_L)^2 &= \sum_{j=1}^{N_L}\epsilon_{L_j}^2 - N_L\mu_L^2 \\ &= \sum_{j=1}^{N_L-1}\epsilon_{L_j}^2 - N_L\mu_L^2 + \epsilon_{L_{N_L}}^2. \end{aligned}$$

The term $N_L\mu_L^2$ may be expressed as

$$\begin{aligned} N_L\mu_L^2 &= N_L\left(\frac{1}{N_L}\sum_{j=1}^{N_L}\epsilon_{L_j}\right)^2 \\ &= \frac{1}{N_L}\left(\sum_{j=1}^{N_L-1}\epsilon_{L_j}+\epsilon_{L_{N_L}}\right)^2 \\ &= \frac{1}{N_L}\left[\left(N_L-1\right)\mu'_L+\epsilon_{L_{N_L}}\right]^2 \\ &= \frac{\left(N_L-1\right)^2\mu'^2_L}{N_L} + \frac{2(N_L-1)\mu'_L\epsilon_{L_{N_L}}}{N_L} + \frac{\epsilon_{L_{N_L}}^2}{N_L} \end{aligned}$$

$$= (N_L-1)\,\mu_L'^2 - \frac{(N_L-1)\,\mu_L'^2}{N_L} + \frac{2(N_L-1)\mu_L'\epsilon_{L,N_L}}{N_L} + \frac{\epsilon_{L_{N_L}}^2}{N_L} + \epsilon_{L_{N_L}}^2 - \epsilon_{L_{N_L}}^2$$
$$= (N_L-1)\,\mu_L'^2 - \frac{(N_L-1)}{N_L}(\epsilon_{L_{N_L}} - \mu_L')^2 + \epsilon_{L_{N_L}}^2.$$

Substituting back in the second term of J_L yields

$$\sum_{j=1}^{N_L}(\epsilon_{L_j}-\mu_L)^2 = \sum_{j=1}^{N_L-1}(\epsilon_{L_j}-\mu_L')^2 + \frac{(N_L-1)}{N_L}(\epsilon_{L_{N_L}}-\mu_L')^2.$$

Substituting back in J_L yields

$$J_L = a + \sum_{j=1}^{N_L-1}(\epsilon_{L_j}-\mu_L')^2 + \frac{(N_L-1)}{N_L}(\epsilon_{L_{N_L}}-\mu_L')^2$$
$$= J_{L+1} + \frac{(N_L-1)}{N_L}(\epsilon_{L_{N_L}}-\mu_L')^2.$$

Since $\frac{(N_L-1)}{N_L}(\epsilon_{L_{N_L}}-\mu_L')^2 \geq 0$, then $J_L \geq J_{L+1}$. □

From Theorem VI.1, it can be implied that $\|\boldsymbol{\Psi}\boldsymbol{\epsilon}(k)\|_2^2$ is minimized when $L = N-2$, i.e., the maximum number of clusters is used. This also implies that using more SOP clusters will decrease $\|\boldsymbol{\Psi}\boldsymbol{\epsilon}(k_0)\|_2^2$ in the upper bound expression of $J(\boldsymbol{\Gamma})$ given in (17).

Theorem VI.2. *Consider $N \geq 3$ carrier phase measurements for estimating the receiver's position $\boldsymbol{r}_r$ and a clustering of L clock states $c\boldsymbol{\delta}t$. Adding a carrier phase measurement from an additional cellular SOP while augmenting the clock state vector $c\boldsymbol{\delta}t$ by its corresponding additional clock state will neither change the position error nor the position error uncertainty.*

Proof. The augmented Jacobian matrix is given by

$$\mathbf{H}' = \begin{bmatrix} \mathbf{G} & \boldsymbol{\Gamma} & \mathbf{0} \\ \boldsymbol{g}^\mathsf{T} & \mathbf{0}^\mathsf{T} & 1 \end{bmatrix},$$

where $\boldsymbol{g} \triangleq \frac{\hat{\boldsymbol{r}}_r - \boldsymbol{r}_{s_{N+1}}}{\left\|\hat{\boldsymbol{r}}_r - \boldsymbol{r}_{s_{N+1}}\right\|_2}$. The new information matrix is subsequently given by

$$\mathbf{H}'^\mathsf{T}\mathbf{H}' = \begin{bmatrix} \mathbf{G}^\mathsf{T}\mathbf{G} + \boldsymbol{g}\boldsymbol{g}^\mathsf{T} & \mathbf{G}^\mathsf{T}\boldsymbol{\Gamma} & \boldsymbol{g} \\ \boldsymbol{\Gamma}^\mathsf{T}\mathbf{G} & \boldsymbol{\Gamma}^\mathsf{T}\boldsymbol{\Gamma} & \mathbf{0} \\ \boldsymbol{g}^\mathsf{T} & \mathbf{0}^\mathsf{T} & 1 \end{bmatrix} = \begin{bmatrix} \mathbf{M}_{11} & \boldsymbol{m}_{12} \\ \boldsymbol{m}_{12}^\mathsf{T} & 1 \end{bmatrix},$$

where

$$\mathbf{M}_{11} \triangleq \begin{bmatrix} \mathbf{G}^\mathsf{T}\mathbf{G} + \boldsymbol{g}\boldsymbol{g}^\mathsf{T} & \mathbf{G}^\mathsf{T}\boldsymbol{\Gamma} \\ \boldsymbol{\Gamma}^\mathsf{T}\mathbf{G} & \boldsymbol{\Gamma}^\mathsf{T}\boldsymbol{\Gamma} \end{bmatrix}, \boldsymbol{m}_{12} \triangleq \begin{bmatrix} \boldsymbol{g} \\ \mathbf{0} \end{bmatrix}.$$

The new covariance is given by

$$\mathbf{P}' = \left(\mathbf{H}'^\mathsf{T}\mathbf{H}'\right)^{-1} = \begin{bmatrix} \mathbf{A}' & \boldsymbol{b}' \\ \boldsymbol{b}'^\mathsf{T} & d' \end{bmatrix},$$

where

$$\mathbf{A}' = \left(\mathbf{M}_{11} - \boldsymbol{m}_{12}\boldsymbol{m}_{12}^\mathsf{T}\right)^{-1}$$
$$\boldsymbol{b}' = -\left(\mathbf{M}_{11} - \boldsymbol{m}_{12}\boldsymbol{m}_{12}^\mathsf{T}\right)^{-1}\boldsymbol{m}_{12}$$
$$d' = 1 + \boldsymbol{m}_{12}^\mathsf{T}\left(\mathbf{M}_{11} - \boldsymbol{m}_{12}\boldsymbol{m}_{12}^\mathsf{T}\right)^{-1}\boldsymbol{m}_{12}$$

The matrix $\mathbf{A}'$ may be expressed as

$$\mathbf{A}' = \left(\begin{bmatrix} \mathbf{G}^\mathsf{T}\mathbf{G} + \boldsymbol{g}\boldsymbol{g}^\mathsf{T} & \mathbf{G}^\mathsf{T}\boldsymbol{\Gamma} \\ \boldsymbol{\Gamma}^\mathsf{T}\mathbf{G} & \boldsymbol{\Gamma}^\mathsf{T}\boldsymbol{\Gamma} \end{bmatrix} - \begin{bmatrix} \boldsymbol{g}\boldsymbol{g}^\mathsf{T} & \mathbf{0} \\ \mathbf{0}^\mathsf{T} & \mathbf{0} \end{bmatrix}\right)^{-1}$$
$$= \begin{bmatrix} \mathbf{G}^\mathsf{T}\mathbf{G} & \mathbf{G}^\mathsf{T}\boldsymbol{\Gamma} \\ \boldsymbol{\Gamma}^\mathsf{T}\mathbf{G} & \boldsymbol{\Gamma}^\mathsf{T}\boldsymbol{\Gamma} \end{bmatrix}^{-1} = \mathbf{P},$$

which indicates that the new uncertainty in the position state is unchanged. The new covariance can be expressed as

$$\mathbf{P}' = \begin{bmatrix} \mathbf{P} & -\mathbf{P}\boldsymbol{m}_{12} \\ -\boldsymbol{m}_{12}^\mathsf{T}\mathbf{P} & 1 + \boldsymbol{m}_{12}^\mathsf{T}\mathbf{P}\boldsymbol{m}_{12} \end{bmatrix} = \begin{bmatrix} \mathbf{P}'_{11} & \mathbf{P}'_{12} & \mathbf{P}'_{13} \\ \mathbf{P}'^\mathsf{T}_{12} & \mathbf{P}'_{22} & \mathbf{P}'_{23} \\ \mathbf{P}'^\mathsf{T}_{13} & \mathbf{P}'^\mathsf{T}_{23} & \mathbf{P}'_{33} \end{bmatrix},$$

where

$$\mathbf{P}'_{11} = \left(\mathbf{G}^\mathsf{T}\boldsymbol{\Psi}\mathbf{G}\right)^{-1}$$
$$\mathbf{P}'_{12} = -\left(\mathbf{G}^\mathsf{T}\boldsymbol{\Psi}\mathbf{G}\right)^{-1}\mathbf{G}^\mathsf{T}\boldsymbol{\Gamma}\left(\boldsymbol{\Gamma}^\mathsf{T}\boldsymbol{\Gamma}\right)^{-1}$$
$$\mathbf{P}'_{13} = -\left(\mathbf{G}^\mathsf{T}\boldsymbol{\Psi}\mathbf{G}\right)^{-1}\boldsymbol{g}$$
$$\mathbf{P}'_{22} = \left(\boldsymbol{\Gamma}^\mathsf{T}\boldsymbol{\Gamma}\right)^{-1}\boldsymbol{\Gamma}^\mathsf{T}\left[\mathbf{I} + \mathbf{G}\left(\mathbf{G}^\mathsf{T}\boldsymbol{\Psi}\mathbf{G}\right)^{-1}\mathbf{G}^\mathsf{T}\right]\boldsymbol{\Gamma}\left(\boldsymbol{\Gamma}^\mathsf{T}\boldsymbol{\Gamma}\right)^{-1}$$
$$\mathbf{P}'_{23} = \left(\boldsymbol{\Gamma}^\mathsf{T}\boldsymbol{\Gamma}\right)^{-1}\boldsymbol{\Gamma}^\mathsf{T}\mathbf{G}\left(\mathbf{G}^\mathsf{T}\boldsymbol{\Psi}\mathbf{G}\right)^{-1}\boldsymbol{g}$$
$$\mathbf{P}'_{33} = 1 + \boldsymbol{g}^\mathsf{T}\left(\mathbf{G}^\mathsf{T}\boldsymbol{\Psi}\mathbf{G}\right)^{-1}\boldsymbol{g}$$

The new estimation error is given by

$$\delta\boldsymbol{r}'_r(k) = -\mathbf{P}'\mathbf{H}'^\mathsf{T}\boldsymbol{\epsilon}'(k),$$

where $\boldsymbol{\epsilon}'(k) \triangleq \left[\boldsymbol{\epsilon}^\mathsf{T}(k), \epsilon_{N+1}(k)\right]^\mathsf{T}$ and $\epsilon_{N+1}(k)$ is the error from the $(N+1)^{\text{st}}$ measurement. Using the expressions of $\mathbf{P}'$, $\mathbf{H}'$, and $\boldsymbol{\epsilon}'$, it can be readily shown that

$$\delta\boldsymbol{r}'_r(k) = -\left(\mathbf{G}^\mathsf{T}\boldsymbol{\Psi}\mathbf{G}\right)^{-1}\mathbf{G}^\mathsf{T}\boldsymbol{\Psi}\boldsymbol{\epsilon}(k) = \delta\boldsymbol{r}_r(k).$$

Therefore, the addition of a measurement while augmenting the clock state vector by one state will not improve the position estimate nor the position error uncertainty. □

From Theorem VI.2, it can be implied that it is required that $N_l \geq 2$ in order for cluster l to contribute in estimating the position state. Therefore, $\lambda_{\max}\left(\mathbf{P}_{x,y}\right)$ can be made smaller by decreasing the number of clusters L. Combining the conclusions of Theorems VI.1 and VI.2 and referring to (17), one can see that there is a tradeoff between estimating more clock biases and uncertainty reduction: less bias for more uncertainty and vice versa. Subsequently, a good rule of thumb is to have at least on cluster with $N_l \geq 3$ (to ensure observability) and $N_l \geq 2$ for the remaining clusters. This implies that $L \leq \frac{N-3}{2} + 1$, which significantly reduces the number of possible clusters in the exhaustive search algorithm.

D. Upper Bound on the Position Error

Note that for a given number of SOPs, one will choose a clustering that will yield a performance that is at least as good as estimating one clock bias. Therefore, a bound on the position error may be established according to

$$\|\delta\boldsymbol{r}_r(k)\|_2 \leq \left\|\left(\mathbf{G}^\mathsf{T}\boldsymbol{\Psi}_1\mathbf{G}\right)^{-1}\mathbf{G}^\mathsf{T}\boldsymbol{\Psi}_1\boldsymbol{\epsilon}(k)\right\|_2,$$

where $\boldsymbol{\Psi}_1 \triangleq \mathbf{I} - \frac{1}{N}\mathbf{1}_N\mathbf{1}_N^\mathsf{T}$.

VII. Experimental Results

In this section, experimental results are presented demonstrating precise, sub-meter level UAV navigation results via the two frameworks developed in this paper: (1) CD-cellular with a mapper/navigator and (2) single UAV with precise carrier phase measurements. As mentioned in Section III, only the 2–D positions of the UAVs are estimated as their height may be obtained using other sensors (e.g., altimeter). In the following experiments, the height of the UAVs was obtained from their on-board navigation systems. Moreover, the noise equivalent bandwidth of the receivers' PLL was set to $B_{\mathrm{N,PLL}} = B_{\mathrm{M,PLL}} = B_{\mathrm{PLL}} = 3$ Hz in all experiments.

A. Carrier Phase Differential Cellular UAV Navigation Results via the Mapper/Navigator Framework

In order to demonstrate the mapper/navigator framework discussed in Section III, two Autel Robotics X-Star Premium UAVs were equipped each with an Ettus E312 USRP, a consumer-grade 800/1900 MHz cellular antenna, and a small consumer-grade GPS antenna to discipline the on-board oscillator. The receivers were tuned to a 882.75 MHz carrier frequency (i.e., $\lambda = 33.96$ cm), which is a cellular CDMA channel allocated for the U.S. cellular provider Verizon Wireless. Samples of the received signals were stored for offline post-processing. The cellular carrier phase measurements were given at a rate of 37.5 Hz, i.e., $T = 0.0267$ ms. The ground-truth reference for each UAV trajectory was taken from its on-board navigation system, which uses GPS, an inertial measurement unit (IMU), and other sensors. The navigator's total traversed trajectory was 1.72 Km, which was completed in 3 minutes. Over the course of the experiment, the receivers on-board the UAVs were listening to 9 BTSs, whose positions were mapped prior to the experiment according to the framework discussed in [27]. A plot of the carrier-to-noise ratios of all the BTSs measured by the navigator is given in Fig. 9. The mapper measured similar carrier-to-noise values.

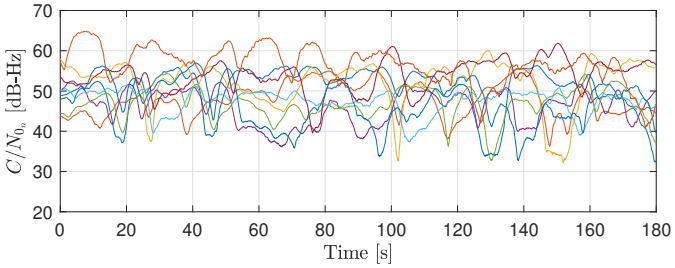

Fig. 9. Carrier-to-noise ratios $\{C/N_{0_n}\}_{n=1}^{9}$ of all the cellular BTSs measured by the navigator. The carrier-to-noise ratios measured by the mapper were of similar values.

The CD-cellular measurements were used to estimate the navigating receiver's trajectory via the mapper/navigator framework developed in Section III. The experimental setup, the SOP BTS layout, and the true and estimated navigator UAV trajectories are shown in Fig. 10. The position RMSE was found to be 63.1 cm. Note that the Least-Squares AMBiguity Decorrelation Adjustment (LAMBDA) method [33] implemented at the Delft University of Technology was used to solve for the integer ambiguities [35].

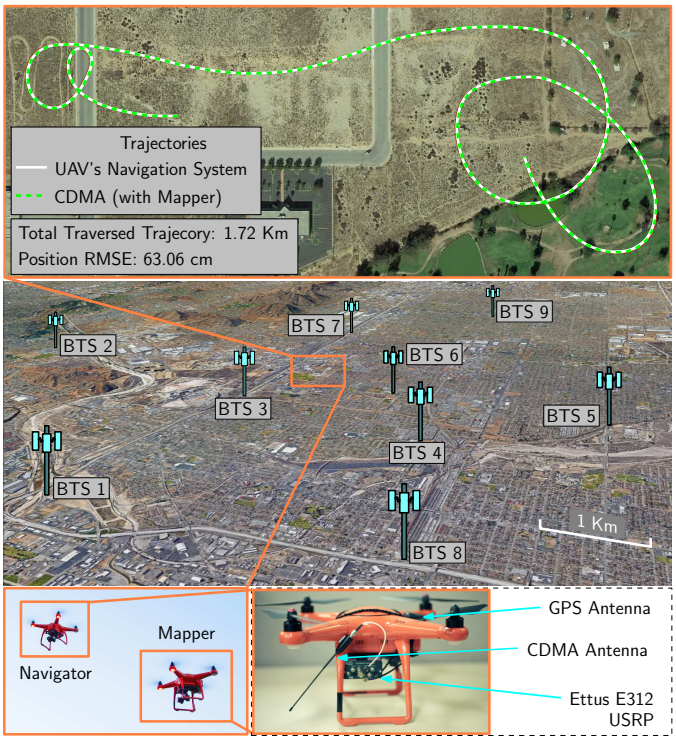

Fig. 10. Experimental setup, the SOP BTS layout, and the true and estimated navigator UAV trajectories via CD-cellular measurements in the mapper/navigator framework. The true and estimated trajectories are shown in solid and dashed lines, respectively. Map data: Google Earth.

B. Single UAV Navigation Results with Precise Cellular Carrier Phase Measurements

Two experiments were conducted at different times. In the first experiment, the same setup described in Subsection VII-A was used, except that the navigator was navigating without the mapper and was employing the framework developed in Section IV. In the second experiment, a DJI Matrice 600 was equipped with the same hardware described in Subsection VII-A and the on-board USRP was tuned to the same carrier frequency. The cellular carrier phase measurements were also given at a rate of 37.5 Hz, i.e., $T = 0.0267$ ms. The ground-truth reference for the UAV trajectory was taken from its on-board navigation system, which also uses GPS, an IMU, and other sensors. The experimental setup and SOP BTS layout for the second experiment are shown in Fig. 11.

In both experiments, the UAVs had access to GPS for 10 seconds, then GPS was cut off. During the time where GPS was available, the cellular signals were used to cluster the cellular SOPs and characterize the clock deviations, as described in Subsection V-B. In the first experiment, the UAV traversed a trajectory of 1.72 Km, which was completed in 3 minutes. The receiver was listening to the same 9 CDMA BTSs as in Fig. 10, with the same carrier-to-noise ratios as in Fig. 9. The navigation results are shown in Fig. 12. The optimal clustering was found to be $\mathcal{C}_1 = \{\mathrm{BTS\,1}, \mathrm{BTS\ 5}, \mathrm{BTS\ 7}, \mathrm{BTS\ 8}\}$,

$\mathcal{C}_2 = \{\text{BTS 2, BTS 3, BTS 6}\}$, and $\mathcal{C}_3 = \{\text{BTS 4, BTS 9}\}$. The position RMSE was calculated to be 36.61 cm.

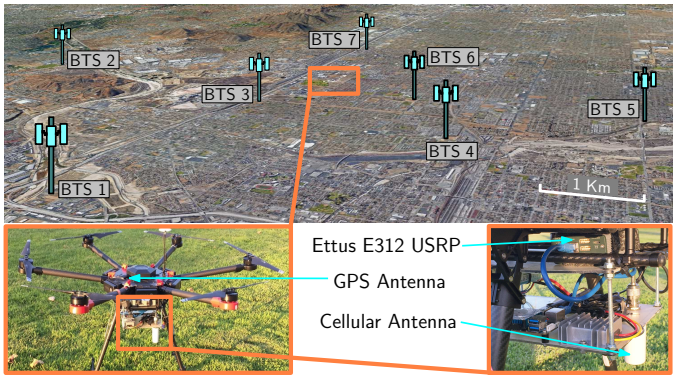

Fig. 11. Experimental setup and the SOP BTS layout for the second experiment demonstrating a single UAV navigating with precise cellular carrier phase measurements. Map data: Google Earth.

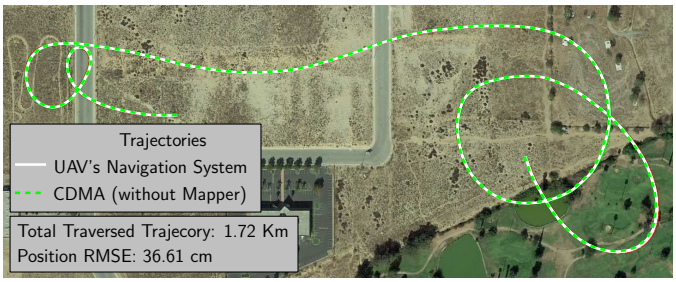

Fig. 12. First experiment demonstrating a single UAV navigating with precise cellular carrier phase measurements. The true and estimated trajectories are shown in solid and dashed lines, respectively. Map data: Google Earth.

In the second experiment, the UAV traversed a trajectory of 3.07 Km completed in 325 seconds. The receiver was listening to the 7 CDMA BTSs shown in Fig. 11. The carrier-to-noise ratios of all the BTSs measured by the navigating UAV in the second experiment are given in Fig. 13 and the navigation results are shown in Fig. 14. The optimal clustering was found to be $\mathcal{C}_1 = \{\text{BTS 1, BTS 2, BTS 3, BTS 4, BTS 6}\}$ and $\mathcal{C}_2 = \{\text{BTS 5, BTS 7}\}$. The position RMSE was calculated to be 88.58 cm.

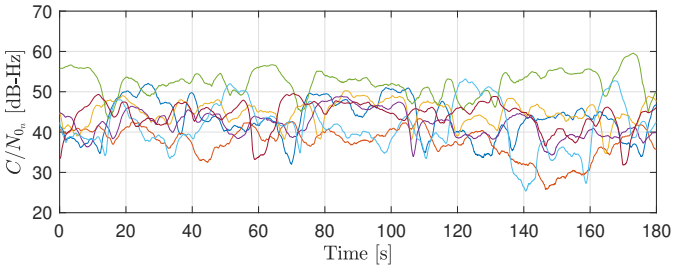

Fig. 13. Carrier-to-noise ratios of all $\{C/N_{0_n}\}_{n=1}^{7}$ the cellular BTSs measured by the navigating UAV for the second experiment.

The experimental results are summarized in Table I.

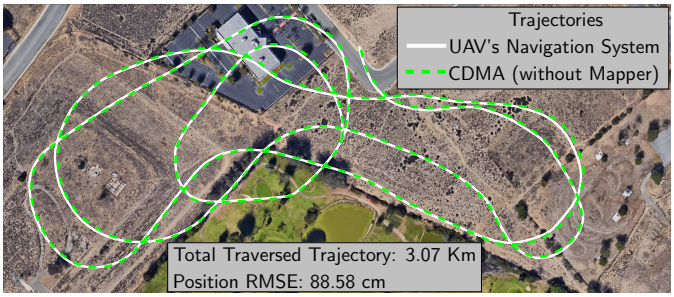

Fig. 14. Second experiment demonstrating a single UAV navigating with precise cellular carrier phase measurements. The true and estimated trajectories are shown in solid and dashed lines, respectively. Map data: Google Earth.

TABLE I
EXPERIMENTAL RESULTS

Framework	**Experiment 1 RMSE [cm]**	**Experiment 2 RMSE [cm]**
CD-Cellular with Mapper/Navigator	63.06	–
Single UAV	36.61	88.58

C. Discussion

First, it is important to note that all RMSEs were calculated with respect to the trajectory returned by the UAVs' on-board navigation system. Although these systems use multiple sensors for navigation, they are not equipped with high precision GPS receivers, e.g., Real Time Kinematic (RTK) systems. Therefore, some errors are expected in what is considered to be "true" trajectories taken from the on-board sensors. The hovering horizontal precision of the UAVs are reported to be 2 meters for the X-Star Premium by Autel Robotics and 1.5 meters for the Matrice 600 by DJI.

Second, it can be noted that the CD-cellular with mapper/navigator framework under-performed compared to the single UAV framework. This can be due to: (1) poor synchronization between the mapper's and navigator measurements and (2) errors in the mapper position. It is important to note that the mapper was mobile during the experiment and the position returned by its on-board navigation system was used as ground-truth. Consequently, any errors in the GPS solution would have degraded the navigator's estimate.

Third, the RMSEs reported in this section are for optimal clustering. In the 10 seconds during which GPS was available, a search was performed to optimally cluster the clock biases using the rule-of-thumb discussed in Subsection VI-C. The search took less than 3 seconds. The RMSEs without clustering (only one bias is estimated) are 48 cm and 97 cm for the first and second experiments, respectively.

VIII. CONCLUSION

This paper presented two frameworks for precise UAV navigation with cellular carrier phase measurements. The first framework relies on a mapping UAV and a navigating UAV. Both UAVs are making carrier phase measurements to the same cellular SOPs and share these estimates to produce the double difference carrier phase measurement. During the

period when GPS is available, the UAVs use their carrier phase measurements and known position to estimate the integer ambiguities. Once GPS is cutoff, the navigator can produce an estimate of its position. Experimental results showed a 63.06 cm position RMSE with this framework.

The second framework leverages the relative stability of cellular BTSs clocks. This stability also allows to parameterize the SOP clock biases by a common term plus some small deviations from the common term, which alleviates the need for a mapper. The clock deviations were subsequently modeled as a stochastic sequence using experimental data. Next, performance bounds were established for this framework. Experimental data show that a single UAV can navigate with sub-meter level accuracy for more than 5 minutes using this framework, with one experiment showing 36.61 cm position RMSE and another showing 88.58 cm position RMSE.

ACKNOWLEDGMENT

The authors would like to thank Joshua Morales for his help in data collection.

REFERENCES

[1] J. Seo, Y. Chen, D. De Lorenzo, S. Lo, P. Enge, D. Akos, and J. Lee, "A real-time capable software-defined receiver using GPU for adaptive anti-jam GPS sensors," *Sensors*, vol. 11, no. 9, pp. 8966–8991, September 2011.

[2] A. Kerns, D. Shepard, J. Bhatti, and T. Humphreys, "Unmanned aircraft capture and control via GPS spoofing," *Journal of Field Robotics*, vol. 31, no. 4, pp. 617–636, 2014.

[3] D. He, S. Chan, and M. Guizani, "Communication security of unmanned aerial vehicles," *IEEE Wireless Communications*, vol. 24, no. 4, pp. 134–139, August 2017.

[4] J. McEllroy, "Navigation using signals of opportunity in the AM transmission band," Master's thesis, Air Force Institute of Technology, Wright-Patterson Air Force Base, Ohio, USA, 2006.

[5] S. Fang, J. Chen, H. Huang, and T. Lin, "Is FM a RF-based positioning solution in a metropolitan-scale environment? A probabilistic approach with radio measurements analysis," *IEEE Transactions on Broadcasting*, vol. 55, no. 3, pp. 577–588, September 2009.

[6] M. Joerger, L. Gratton, B. Pervan, and C. Cohen, "Analysis of Iridium-augmented GPS for floating carrier phase positioning," *NAVIGATION, Journal of the Institute of Navigation*, vol. 57, no. 2, pp. 137–160, 2010.

[7] K. Pesyna, Z. Kassas, and T. Humphreys, "Constructing a continuous phase time history from TDMA signals for opportunistic navigation," in *Proceedings of IEEE/ION Position Location and Navigation Symposium*, April 2012, pp. 1209–1220.

[8] R. Faragher, C. Sarno, and M. Newman, "Opportunistic radio SLAM for indoor navigation using smartphone sensors," in *Proceedings of IEEE/ION Position Location and Navigation Symposium*, April 2012, pp. 120–128.

[9] I. Bisio, M. Cerruti, F. Lavagetto, M. Marchese, M. Pastorino, A. Randazzo, and A. Sciarrone, "A trainingless WiFi fingerprint positioning approach over mobile devices," *IEEE Antennas and Wireless Propagation Letters*, vol. 13, pp. 832–835, 2014.

[10] W. Xu, M. Huang, C. Zhu, and A. Dammann, "Maximum likelihood TOA and OTDOA estimation with first arriving path detection for 3GPP LTE system," *Transactions on Emerging Telecommunications Technologies*, vol. 27, no. 3, pp. 339–356, 2016.

[11] A. Tahat, G. Kaddoum, S. Yousefi, S. Valaee, and F. Gagnon, "A look at the recent wireless positioning techniques with a focus on algorithms for moving receivers," *IEEE Access*, vol. 4, pp. 6652–6680, 2016.

[12] K. Shamaei, J. Khalife, and Z. Kassas, "Exploiting LTE signals for navigation: Theory to implementation," *IEEE Transactions on Wireless Communications*, vol. 17, no. 4, pp. 2173–2189, April 2018.

[13] J. Khalife and Z. Kassas, "Navigation with cellular CDMA signals – part II: Performance analysis and experimental results," *IEEE Transactions on Signal Processing*, vol. 66, no. 8, pp. 2204–2218, April 2018.

[14] C. Gentner, T. Jost, W. Wang, S. Zhang, A. Dammann, and U. Fiebig, "Multipath assisted positioning with simultaneous localization and mapping," *IEEE Transactions on Wireless Communications*, vol. 15, no. 9, pp. 6104–6117, September 2016.

[15] P. Muller, J. del Peral-Rosado, R. Piche, and G. Seco-Granados, "Statistical trilateration with skew-t distributed errors in LTE networks," *IEEE Transactions on Wireless Communications*, vol. 15, no. 10, pp. 7114–7127, October 2016.

[16] Z. Kassas, J. Morales, K. Shamaei, and J. Khalife, "LTE steers UAV," *GPS World Magazine*, vol. 28, no. 4, pp. 18–25, April 2017.

[17] Z. Kassas, J. Khalife, K. Shamaei, and J. Morales, "I hear, therefore I know where I am: Compensating for GNSS limitations with cellular signals," *IEEE Signal Processing Magazine*, pp. 111–124, September 2017.

[18] J. del Peral-Rosado, J. Lopez-Salcedo, G. Seco-Granados, F. Zanier, P. Crosta, R. Ioannides, and M. Crisci, "Software-defined radio LTE positioning receiver towards future hybrid localization systems," in *Proceedings of International Communication Satellite Systems Conference*, October 2013, pp. 14–17.

[19] C. Yang, T. Nguyen, and E. Blasch, "Mobile positioning via fusion of mixed signals of opportunity," *IEEE Aerospace and Electronic Systems Magazine*, vol. 29, no. 4, pp. 34–46, April 2014.

[20] J. Khalife, K. Shamaei, and Z. Kassas, "A software-defined receiver architecture for cellular CDMA-based navigation," in *Proceedings of IEEE/ION Position, Location, and Navigation Symposium*, April 2016, pp. 816–826.

[21] K. Shamaei, J. Khalife, S. Bhattacharya, and Z. Kassas, "Computationally efficient receiver design for mitigating multipath for positioning with LTE signals," in *Proceedings of ION GNSS Conference*, September 2017, pp. 3751–3760.

[22] Z. Kassas, "Analysis and synthesis of collaborative opportunistic navigation systems," Ph.D. dissertation, The University of Texas at Austin, USA, 2014.

[23] C. Yang and A. Soloviev, "Simultaneous localization and mapping of emitting radio sources-SLAMERS," in *Proceedings of ION GNSS Conference*, September 2015, pp. 2343–2354.

[24] C. Gentner, B. Ma, M. Ulmschneider, T. Jost, and A. Dammann, "Simultaneous localization and mapping in multipath environments," in *Proceedings of IEEE/ION Position Location and Navigation Symposium*, April 2016, pp. 807–815.

[25] J. Morales, P. Roysdon, and Z. Kassas, "Signals of opportunity aided inertial navigation," in *Proceedings of ION GNSS Conference*, September 2016, pp. 1492–1501.

[26] J. Morales and Z. Kassas, "Information fusion strategies for collaborative radio SLAM," in *Proceedings of IEEE/ION Position Location and Navigation Symposium*, April 2018, submitted.

[27] J. Morales and Z. Kassas, "Optimal collaborative mapping of terrestrial transmitters: receiver placement and performance characterization," *IEEE Transactions on Aerospace and Electronic Systems*, vol. 54, no. 2, pp. 992–1007, April 2018.

[28] J. Khalife and Z. Kassas, "Evaluation of relative clock stability in cellular networks," in *Proceedings of ION GNSS Conference*, September 2017, pp. 2554–2559.

[29] 3GPP2, "Physical layer standard for cdma2000 spread spectrum systems (C.S0002-E)," 3rd Generation Partnership Project 2 (3GPP2), TS C.S0002-E, June 2011.

[30] 3GPP, "Evolved universal terrestrial radio access (E-UTRA); physical channels and modulation," 3rd Generation Partnership Project (3GPP), TS 36.211, January 2011. [Online]. Available: http://www.3gpp.org/ftp/Specs/html-info/36211.htm

[31] K. Shamaei, J. Khalife, and Z. Kassas, "Performance characterization of positioning in LTE systems," in *Proceedings of ION GNSS Conference*, September 2016, pp. 2262–2270.

[32] P. Misra and P. Enge, *Global Positioning System: Signals, Measurements, and Performance*, 2nd ed. Ganga-Jamuna Press, 2010.

[33] P. J. G. Teunissen, "The least-squares ambiguity decorrelation adjustment: a method for fast gps integer ambiguity estimation," *Journal of Geodesy*, vol. 70, no. 1, pp. 65–82, November 1995.

[34] L. Ljung, *System identification: Theory for the user*, 2nd ed. Prentice Hall PTR, 1999.

[35] S. Verhagen and B. Li, "LAMBDA software package - MATLAB implementation, version 3.0. Delft Uuniversity of Technology," 2012.